



ARL-TR-7647 • APR 2015



# Imaging Detonations of Explosives

by Kevin L McNesby, Matthew M Biss, Barrie E Homan,  
Richard A Benjamin, Vincent M Boyle Sr, and John M  
Densmore

Approved for public release; distribution is unlimited.

## **NOTICES**

### **Disclaimers**

The findings in this report are not to be construed as an official Department of the Army position unless so designated by other authorized documents.

Citation of manufacturer's or trade names does not constitute an official endorsement or approval of the use thereof.

Destroy this report when it is no longer needed. Do not return it to the originator.



# **Imaging Detonations of Explosives**

**by Kevin L McNesby, Matthew M Biss, Barrie E Homan,  
Richard A Benjamin and Vincent M Boyle Sr**  
*Weapons and Materials Research Directorate, ARL*

**John M Densmore**  
*Lawrence Livermore National Laboratory  
Livermore, CA*

REPORT DOCUMENTATION PAGE				Form Approved OMB No. 0704-0188	
<p>Public reporting burden for this collection of information is estimated to average 1 hour per response, including the time for reviewing instructions, searching existing data sources, gathering and maintaining the data needed, and completing and reviewing the collection information. Send comments regarding this burden estimate or any other aspect of this collection of information, including suggestions for reducing the burden, to Department of Defense, Washington Headquarters Services, Directorate for Information Operations and Reports (0704-0188), 1215 Jefferson Davis Highway, Suite 1204, Arlington, VA 22202-4302. Respondents should be aware that notwithstanding any other provision of law, no person shall be subject to any penalty for failing to comply with a collection of information if it does not display a currently valid OMB control number.</p> <p><b>PLEASE DO NOT RETURN YOUR FORM TO THE ABOVE ADDRESS.</b></p>					
1. REPORT DATE (DD-MM-YYYY) April 2016		2. REPORT TYPE Final		3. DATES COVERED (From - To) October 2012–October 2015	
4. TITLE AND SUBTITLE Imaging Detonations of Explosives				5a. CONTRACT NUMBER	
				5b. GRANT NUMBER	
				5c. PROGRAM ELEMENT NUMBER	
6. AUTHOR(S) Kevin L McNesby, Matthew M Biss, Barrie E Homan, Richard A Benjamin, Vincent M Boyle Sr, and John M Densmore				5d. PROJECT NUMBER	
				5e. TASK NUMBER	
				5f. WORK UNIT NUMBER	
7. PERFORMING ORGANIZATION NAME(S) AND ADDRESS(ES) US Army Research Laboratory ATTN: RDRL-WML-C Aberdeen Proving Ground, MD 21005-5069				8. PERFORMING ORGANIZATION REPORT NUMBER  ARL-TR-7647	
9. SPONSORING/MONITORING AGENCY NAME(S) AND ADDRESS(ES)				10. SPONSOR/MONITOR'S ACRONYM(S)	
				11. SPONSOR/MONITOR'S REPORT NUMBER(S)	
12. DISTRIBUTION/AVAILABILITY STATEMENT Approved for public release; distribution is unlimited.					
13. SUPPLEMENTARY NOTES					
14. ABSTRACT <p>The techniques and instrumentation presented in this report allow for mapping of temperature, pressure, chemical species, and energy deposition during and following detonations of explosives. Developed over the last several years under US Army mission funding, this work has been transitioned from a developmental task to the regular “toolkit” employed by researchers within the US Army Research Laboratory. This work provides measurement in the explosive near- to far-field (0–500 charge diameters) of surface temperatures, peak air-shock pressures, some chemical species signatures, and shock energy deposition. Information on these events is used to evaluate the performance, lethality, and survivability of Army munitions.</p>					
15. SUBJECT TERMS imaging, explosions, temperature, pressure, chemical species					
16. SECURITY CLASSIFICATION OF:			17. LIMITATION OF ABSTRACT  UU	18. NUMBER OF PAGES  38	19a. NAME OF RESPONSIBLE PERSON Kevin L McNesby
a. REPORT Unclassified	b. ABSTRACT Unclassified	c. THIS PAGE Unclassified			19b. TELEPHONE NUMBER (Include area code) 410-306-1383

## Contents

---

<b>List of Figures</b>	<b>v</b>
<b>List of Tables</b>	<b>vi</b>
<b>1. Introduction</b>	<b>1</b>
<b>2. Pyrometry</b>	<b>1</b>
2.1 Background	1
2.2 Theory	2
2.3 Instrumentation	3
2.4 Results	4
<b>3. Optically Based Pressure Measurement</b>	<b>6</b>
3.1 Background	6
3.2 Theory and Instrumentation	7
3.3 Results	8
<b>4. Chemical Species Imaging</b>	<b>9</b>
4.1 Background	9
4.2 Theory and Approach	10
4.3 Instrumentation	11
4.3.1 2-Camera Image Registration	12
4.3.2 Particle Temperature Measurements	12
4.3.3 Light-Gas Gun	12
4.4 Results	14
4.5 Discussion	16
<b>5. Blast Energy on Target</b>	<b>17</b>
5.1 Introduction	17
5.2 Instrumentation	17
5.3 Imaging	18

5.4 Results	19
<b>6. Summary and Conclusions</b>	<b>22</b>
<b>7. References</b>	<b>23</b>
<b>Distribution List</b>	<b>29</b>

## List of Figures

---

Fig. 1	A schematic of the ARL imaging pyrometer rig as employed for temperature measurements of exploding spheres of the explosive formulation C-4.....	4
Fig. 2	Full-color imaging pyrometry measurements for a 227-g charge of C-4 at 63.5-cm standoff from a metal-surface table used to simulate an armor surface. Time sequence: a<b<c<d<e<f with a time interval of 71 $\mu$ s between frames. X- and y-axes labels are in millimeters. Color chart bar indicates temperature in Kelvin. ....	5
Fig. 3	A frame from a temperature movie of a fireball produced by a 1,000-g TNT charge encased in a boron/polymer matrix. The field of view of the camera is approximately 2 m; the frame is approximately 100 $\mu$ s after initiation. The color temperature scale is in Kelvin. The field of view is approximately 1 m <sup>2</sup> . Color chart bar indicates temperature in Kelvin.....	6
Fig. 4	An image sequence of center-detonated exploding, 300-g C-4 spheres measured using a high-speed framing camera. Exposure time per picture is 300 ns, and the time between each exposure is approximately 1 $\mu$ s.....	8
Fig. 5	Optically based peak shock pressure measurements using the framing camera (Cordin Model 570) and the streak camera rig, and predictions based upon CONWEP. The data is from the images shown in Fig. 4.....	9
Fig. 6	Emission from a burning 1:1 (by weight) powder mixture of a milspec B/KNO <sub>3</sub> (MIL-STD-961) igniter formulation. Spectral lines from gaseous BO <sub>2</sub> emission (arrows) appear superimposed upon particle incandescence. Not corrected for intensity response of the spectrograph. ....	11
Fig. 7	Schematic of the gas-gun catch-tank assembly. The photograph of the impact event is a single frame from a color camera mounted at the top of the catch tank assembly. ....	13
Fig. 8	The 2-camera rig in position at the side port of the catch tank prior to a gun firing. Note the color camera at the top port of the catch tank. The gas gun is positioned to the left of the chamber out of the field of view of the photo. The white plastic fixtures in front of each camera lens contain the optical filters.....	14

Fig. 9	A series of processed images, time after impact, that are part of an emission movie to image B oxidation/BO <sub>2</sub> emission. The projectile enters at the left of the figure; the anvil is at the right of the figure. Red indicates thermal emission (incandescence) near a wavelength of 700 nm has higher overall intensity; green indicates emission from incandescence plus BO <sub>2</sub> emission near a wavelength of 546 nm has higher overall intensity. The x and y scales are pixel indices. Each pixel corresponds to approximately 100 μm in length at the focal plane of the 2-camera rig. ....	15
Fig. 10	A plot of particle incandescent temperature and time to onset of gaseous BO <sub>2</sub> emission (i.e., ignition delay) vs. impact velocity for B/KNO <sub>3</sub> -containing polyethylene spheres.....	16
Fig. 11	The low-parallax high-brightness imaging rig. Low parallax is achieved by placing the laser directional mirror at the center of the camera lens.....	18
Fig. 12	A shock wave being reflected by a mannequin. Peak pressure at the visor was approximately 69.5 psi. Charge was 660-g pentolite, 2 m from center of face shield. ....	19
Fig. 13	Incoming vs. reflected shock velocity for Fig. 8. ....	22

## List of Tables

Table 1	Physical parameters of the shock prior to visor .....	20
Table 2	Physical parameters of the shock after reflection by visor .....	21



## **1. Introduction**

---

An effort has been made within the US Army Research Laboratory (ARL) to extract quantitative information on explosive performance from high-speed imaging of explosions. Explosive fireball surface temperatures are measured using imaging pyrometry (2-color 2-camera imaging pyrometer; full-color single-camera imaging pyrometer). Framing cameras are synchronized with pulsed laser illumination to measure fireball/shock expansion velocities, enabling calculation of peak air-shock pressures. Multicamera filtering at different wavelengths enables visualization of light emission by some reactant species participating in energy release during an explosion. Measurement of incident and reflected shock velocities is used to calculate shock energy on target.

Results of these measurements are used to construct maps of temperature, pressure, reactant species, and shock energy on target. This information is valuable to evaluate explosive performance, models of performance, and barriers designed to enhance protection and survivability. These techniques and instruments were developed, in part, to improve productivity by lowering testing costs, allowing a single event to yield temperature, pressure, chemical species, and performance data.

## **2. Pyrometry**

---

### **2.1 Background**

---

Pyrometry is the method of estimating temperature of incandescent bodies from standoff, or noncontact methods. Modern optical techniques for temperature measurement began in the early 1900s using the disappearing-filament technique, where the eye of an operator was used to judge when the red-filtered incandescence from a sample to be measured matched the output from a similarly filtered, resistively heated filament (the filament “disappeared” when the 2 images were superimposed).<sup>1</sup> By 1905, the techniques had advanced to the point of publication of a National Bureau of Standards monograph that described single and 2-color optical pyrometry and was based in part on theoretical work on gray emitters by Planck, Wien, and others.<sup>2</sup> The commercial application of optical pyrometry for the next 50 years relied on the disappearing-filament technique. Accuracy by the 1960s approached 1 °C, over a range of approximately 775–2,850 °C.<sup>3</sup> With the advent of solid-state photodetectors beginning in about 1960, 2-color<sup>4</sup> or “ratio” optical pyrometry began replacing disappearing-filament-based instrumentation.

A requirement of the 2-color color technique is that variance in emissivity with wavelength is small, such that the object in question exhibits gray body behavior.<sup>5</sup> Three-, 4-, and 6-color pyrometry has enabled temperature measurement of materials with wavelength-dependent emissivities, provided that the change is continuous.<sup>6</sup> In 2006, Goroshin et al. used multiwavelength pyrometers to measure temperatures of explosions with microsecond time resolution.<sup>7</sup> Even when accounting for changes in emissivity with wavelength, the spectral region to be investigated should be free of discrete, gas phase emission. Therefore, each temperature measurement should be accompanied by a full emission spectrum. Standoff temperature estimation using the line spectra of gas phase species in emission has been shown to be effective for species that rapidly reach local thermal equilibrium with their surroundings (e.g., some atomic emission).<sup>8</sup> However, fitting discrete spectral features in emission can be risky and for some species yields erroneous values of temperature (e.g., CO emission in some flames).<sup>9</sup>

Extending these techniques to imaging pyrometry employing light-sensitive pixel arrays began in the 1990s with work on thin filament pyrometry.<sup>10</sup> With the advent of fast charged-coupled device (CCD) cameras, it became possible to image temperatures and to follow temperature change in dynamic events (e.g., diesel engine combustion).<sup>11–13</sup> Along with the development of the color CCD camera came single-camera pyrometry that employed a multiwavelength technique using the R-G-B Bayer-type mask for pixel filtering.<sup>14</sup> Kuhn et al. used a Nikon D70 to temperature-map an atmospheric pressure flame.<sup>15</sup> Densmore et al. have applied the 2-color and multiwavelength imaging techniques to explosions.<sup>16,17</sup>

## 2.2 Theory

---

The principle behind most pyrometric techniques is an application of Planck's radiation law (Eq. 1), where  $I_\lambda$  is light intensity at wavelength  $\lambda$ ,  $h$  is Planck's constant,  $c$  is the speed of light,  $k$  is Boltzmann's constant,  $\varepsilon_\lambda$  is the emissivity of the material (wavelength dependent), and  $T$  is the temperature.<sup>18</sup>

$$I_\lambda = 2\varepsilon_\lambda hc^2/\lambda^5 \times 1/[\exp(hc/\lambda kT) - 1] . \quad (1)$$

It is possible to use Eq. 1 to measure the temperature of a body with one detector. However, this is impractical as the intensity of light falling on the detector is highly optical-path dependent and the light transfer function (how the optics modify light throughput) must be carefully characterized.<sup>19</sup> To mitigate this limitation, the intensity of light at 2 or more wavelengths is measured. If the optical paths are similar, the transfer function can be removed from consideration. The ratio of light intensities (Eq. 1) at 2 wavelengths<sup>20</sup> is given by Eq. 2:

$$I_{\lambda 1} / I_{\lambda 2} = [\varepsilon_{\lambda 1} \lambda_2^5 (\exp(hc/\lambda_2 kT) - 1)] / [\varepsilon_{\lambda 2} \lambda_1^5 (\exp(hc/\lambda_1 kT) - 1)] . \quad (2)$$

Because the emissivity  $\varepsilon$  is usually not known for the body under study, it is (often erroneously) assumed to be wavelength independent (gray body assumption) and therefore can be factored out.<sup>21</sup> As the equation is nonlinear, 2 approaches have been investigated to solve Eq. 2 for temperature. The first is to assume that, at the temperatures of interest for detonations, the exponential term is large compared to 1 (Wien's approximation<sup>22</sup>). Dropping one from the numerator and denominator allows for an analytical solution. Alternatively, Eq. 2 is kept intact and a numerical search for the corresponding temperature is performed.<sup>23</sup>

### 2.3 Instrumentation

---

In work described here, time-resolved temperature maps of detonations of explosives are made using a full-color single-camera pyrometer where wavelength resolution is achieved using the Bayer-type mask covering the sensor chip<sup>17</sup> and a 2-color imaging pyrometer employing 2 monochrome cameras filtered at wavelengths of 700 and 900 nm, respectively, (wavelength regions adjustable). Each rig operates on the assumption of gray body behavior described previously, but each is specific to the type of explosive being investigated. For many CHNO-based explosives (e.g., TNT [ $C_7H_5N_3O_6$ ], the formulation C-4 [92% RDX,  $C_3H_6N_6O_6$ ]), hot detonation products are mainly soot and permanent gases, presenting an approximation of a gray body emitter.<sup>7,24</sup> For these systems, the single-camera rig may be appropriate. For metalized explosives, narrow-band light emission from gas phase molecular and atomic species (e.g., AlO near 484 nm,  $BO_2$  near 560 nm, and K near 760 nm) necessitates the use of the 2-camera rig to make measurements in spectral regions free of discrete features. Additionally, strong  $C_2$  or CH emission from nonsooting explosive fireballs may present a significant source of error.<sup>25</sup> For each measurement approach, it is mandatory to measure a time-resolved emission spectrum during the event to ensure the absence of discrete emission in the spectral window used for temperature measurement.<sup>26</sup>

For each pyrometer rig described here, framing speeds are 20,000–40,000 frames per second (fps) at a resolution of approximately  $400 \times 500$  pixels with an exposure per frame of one to tens of microseconds. Each system is temperature calibrated using a standard blackbody source (Omega Engineering), and checked for accuracy using an air/acetylene diffusion flame.<sup>27</sup>

A schematic of the ARL imaging pyrometer rig (showing the 2-camera rig and the full-color rig as described) is shown in Fig. 1, as employed for temperature measurements of exploding 227-gram (g) spheres of the explosive formulation C-4. Also shown in this figure are a spectrograph capable of measuring time-resolved

emission spectra and a 3-color spatially integrating pyrometer used as a check of the imaging devices. The 3-color spatially integrating pyrometer (700, 850, and 1,000 nm; 10-nm bandpass) can provide submicrosecond time resolution but is biased toward measuring the hottest portion of an emitting medium because of the  $T^4$  dependence of intensity.<sup>28</sup>

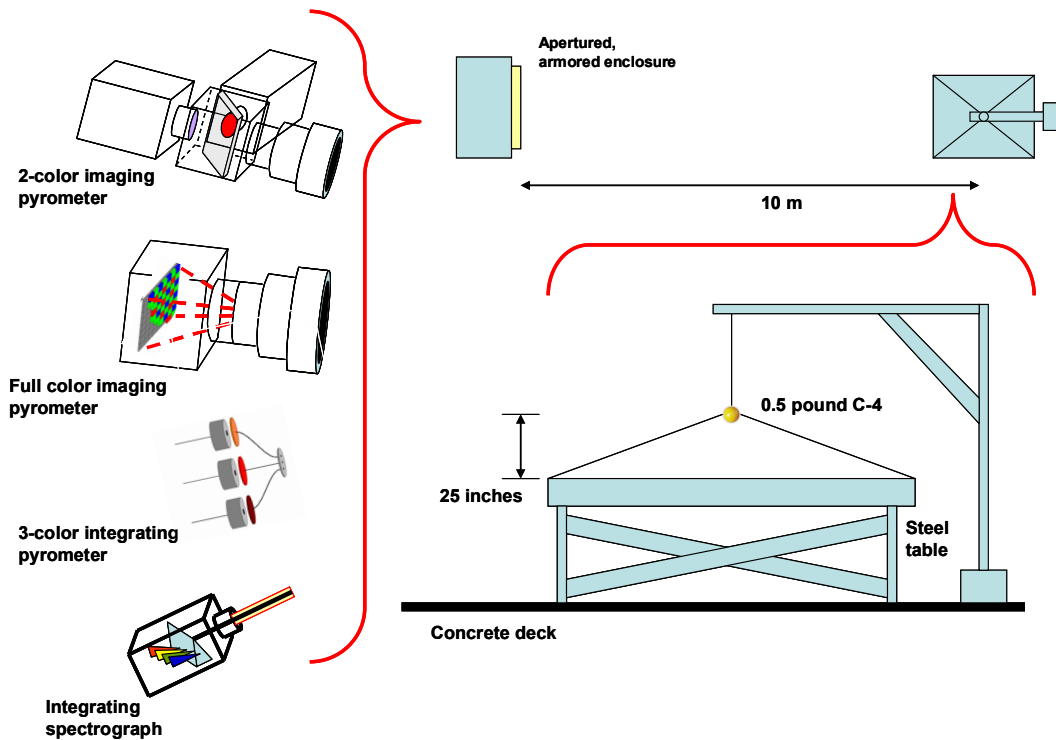
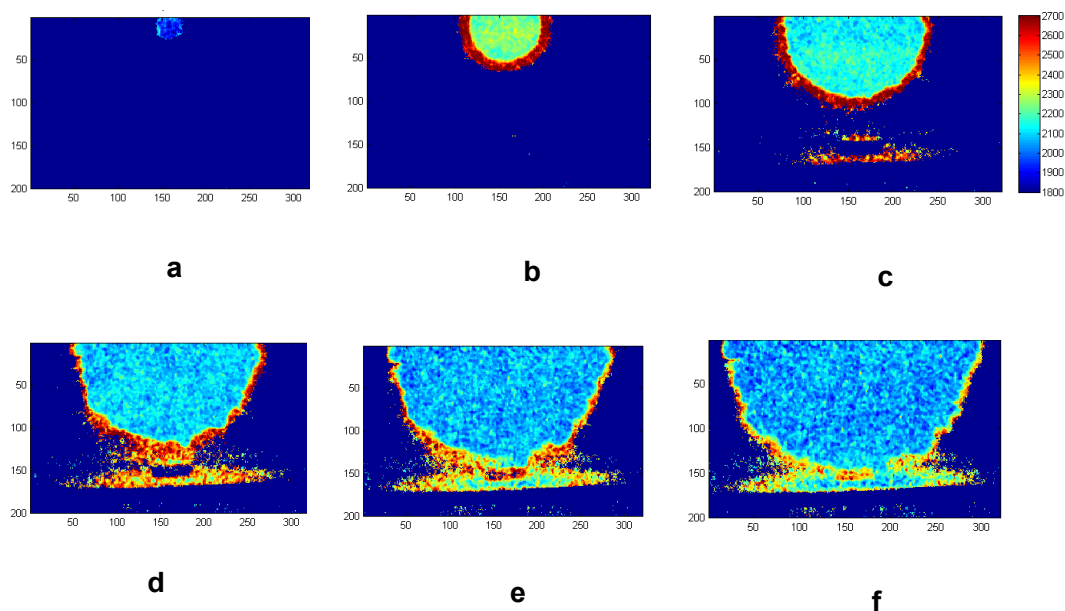


Fig. 1 A schematic of the ARL imaging pyrometer rig as employed for temperature measurements of exploding spheres of the explosive formulation C-4

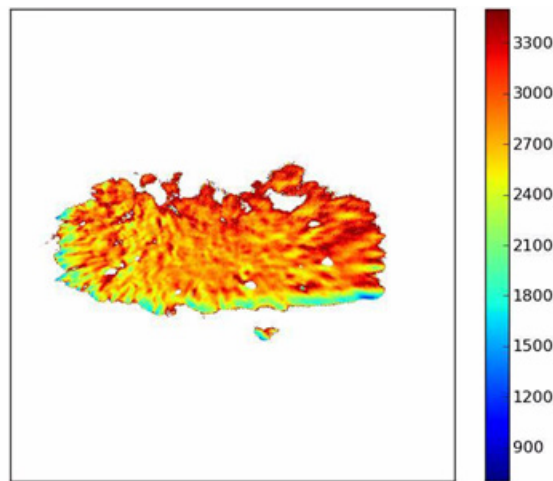
## 2.4 Results

Figure 2 shows a sequence of temperature maps of exploding C-4 spheres in the near-field, measured using the single-camera pyrometer. These images were obtained using the setup shown in Fig 1. Note the hot outer surface of the fireball indicating the primary shock wave location.



**Fig. 2** Full-color imaging pyrometry measurements for a 227-g charge of C-4 at 63.5-cm standoff from a metal-surface table used to simulate an armor surface. Time sequence: a<b<c<d<e<f with a time interval of 71  $\mu$ s between frames. X- and y-axes labels are in millimeters. Color chart bar indicates temperature in Kelvin.

Figure 3 shows a frame from a temperature movie of a fireball produced by detonation of a 1,000-g TNT charge encased in a boron/polymer matrix. Emission bands from  $\text{BO}_2$  near 546 nm mandates the use of the 2-camera rig.<sup>29</sup> Regions of the image in Fig. 3 where no data are shown were either saturated in one or both channels or had intensity levels in one or both channels below the camera noise threshold.



**Fig. 3** A frame from a temperature movie of a fireball produced by a 1,000-g TNT charge encased in a boron/polymer matrix. The field of view of the camera is approximately 2 m; the frame is approximately 100  $\mu$ s after initiation. The color temperature scale is in Kelvin. The field of view is approximately 1 m<sup>2</sup>. Color chart bar indicates temperature in Kelvin.

### 3. Optically Based Pressure Measurement

---

#### 3.1 Background

---

Modern optical pressure measurement methods often rely upon a light-sensitive material placed within the pressure field. Methods include pressure-sensitive fluorescence quenching,<sup>30</sup> pressure-induced shifts in fluorescence wavelengths,<sup>31</sup> pressure-induced changes in interferometer configurations,<sup>32</sup> pressure-sensitive changes in transmission of polarized light through a photoelastic medium,<sup>33</sup> fiber-optic-based Mach-Zender interferometers,<sup>34</sup> and tunable diode laser measurement of pressure-induced changes in absorption line profiles of gases.<sup>35</sup> Standoff optical pressure measurements relating shock velocity to peak shock pressure can trace their origins to the experiments of Hooke, Huygens, Mach, and others, studying heat and flow visualization via changes in refractive index of air,<sup>36</sup> and simultaneous development of high-speed photography. Shock-wave imaging using a short pulse light source in a schlieren system was first demonstrated by Mach and Salcher<sup>37</sup> in 1887. In the early twentieth century, the schlieren technique developed by Mach became the most important tool for visualizing flow during ballistic events. In 1929, the first high-speed schlieren movies (1 million fps for 24 frames) were demonstrated by Cranz and Schardin.<sup>38</sup> The development of high-speed photography by the 1940s focused on high-rotation-speed film<sup>39</sup> or rotating mirrors or prisms.<sup>40</sup> Schlieren imaging became the most important tool for flow

visualization through the 1970s, mainly through work related to supersonic flight and rocket design.<sup>36</sup> Remote measurements of peak pressures in explosions usually rely on measuring shock wave velocities and use Rankine-Hugoniot relations to convert shock Mach numbers to pressures.<sup>41</sup> Improvements in optics and recording techniques, led by the work of Settles et al.,<sup>36</sup> enable highly sensitive measurements of shock position following explosions and of changes in refractive index behind the shock.<sup>42</sup>

Tracking explosively generated shock-wave position using lasers was first reported in the late 1980s.<sup>43</sup> Pulsed copper (Cu)-vapor lasers, synchronized to framing cameras at repetition rates up to 10 kHz, were first reported in 1987.<sup>44</sup> In 2002, Frost et al., using a combination of high-speed imaging and piezo-resistive gauges, reported acceleration of the shock front by metal particle combustion, one of the first investigations of the explosive near-field.<sup>45</sup> In 2005, a 20-kHz Cu vapor laser (510-nm output) was synchronized to a high-speed filtered camera to obtain fireball expansion and shock velocities. Peak pressures calculated from movies of the shock wave agreed reasonably well with pressures reported by mechanical transducers.<sup>46</sup>

### 3.2 Theory and Instrumentation

---

The pressure field of a detonation event is often measured at discrete points in space where gauges are located. Many piezoelectric-based gauge technologies suffer from both thermal effects and fragility.<sup>47–49</sup> This often limits conventional pressure measurements to larger standoff distances ( $\gtrsim 5$  charge diameters). The optical technique used here overcomes these limitations, but is limited in that it cannot provide impulse or pressures within the fireball. However, data from the single or 2-camera pyrometer can capture the fireball and subsequent air shock structure of the detonation event, allowing simultaneous temperature and pressure measurement. Utilizing the Rankine-Hugoniot<sup>29</sup> relationship between shock velocity and shock pressure for a spherical shock expanding into an ideal gas, where  $P_s$  is the shock pressure,  $P_a$  is ambient pressure, and  $M$  is Mach number based on measured shock velocity, the information from the pyrometer can be used to map the pressure field of the explosion (Eq. 3).

$$P_s / P_a = 7[M^2 - 1] / 6 . \quad (3)$$

To calculate shock pressures, it is assumed that at early times (time after detonation of 1 ms or less) the shock wave is coincident with the outer edge of the expanding fireball. At later times, when the air shock has separated from the fireball contact surface, the shock wave position is used to calculate shock velocities.<sup>50</sup> Figure 4 shows an image sequence of center-detonated 300-g exploding C-4 spheres measured using a high-speed framing camera (Cordin Model 570). Exposure time

per picture is 300 ns, and the time between each exposure is approximately 1  $\mu$ s. For longer times and slower expansion velocities, a second digital framing camera (Photron SA-5) was used to record the fireball expansion. Consecutive images are used to determine shock front position versus time, and a peak pressure calculated from measured shock velocities, employing the Rankine-Hugoniot relations (Eq. 3).

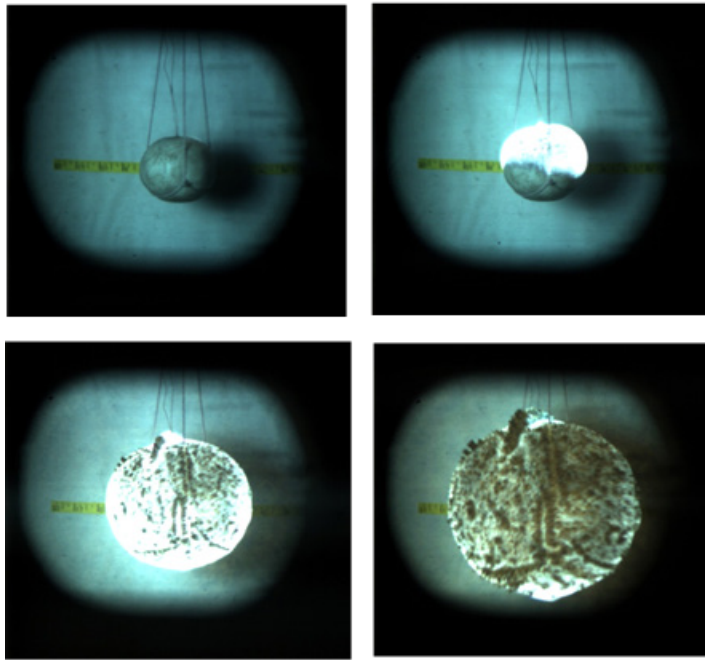


**Fig. 4** An image sequence of center-detonated exploding, 300-g C-4 spheres measured using a high-speed framing camera. Exposure time per picture is 300 ns, and the time between each exposure is approximately 1  $\mu$ s.

### 3.3 Results

---

Figure 5 shows the result of peak shock pressures calculated using data from the high-speed framing cameras (Cordin 570 and Photron SA-5) and results calculated using the blast peak pressure simulator CONWEP.<sup>51</sup> Agreement is reasonable overall. For this multiple camera rig, error in the measurements is believed to be less than 10% at all distances from charge center, with the main sources of error being the duration of exposure (need for even faster cameras at very early times) and deviation from ideal gas behavior at higher Mach number.<sup>29</sup>



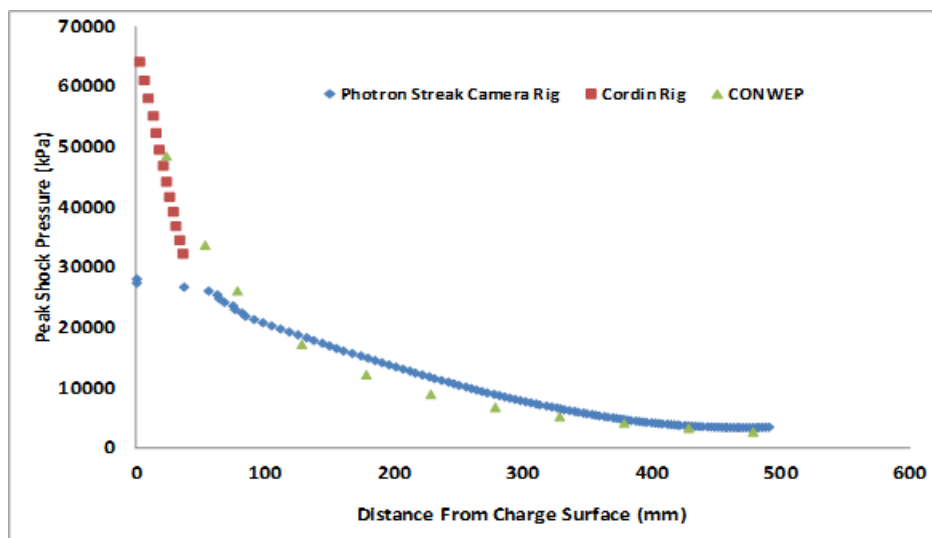
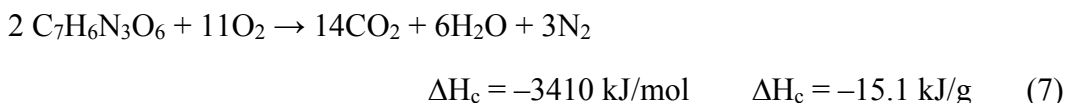
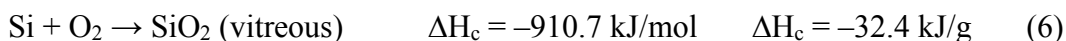
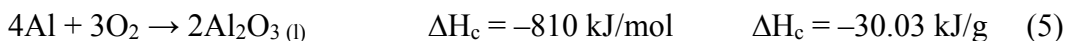
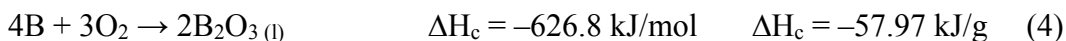


Fig. 5 Optically based peak shock pressure measurements using the framing camera (Cordin Model 570) and the streak camera rig, and predictions based upon CONWEP. The data is from the images shown in Fig. 4.

## 4. Chemical Species Imaging

### 4.1 Background

Several metals and metalloids (e.g., Al [aluminum], B [boron], and Si [silicon]) may be considered for addition to propellants and explosives to increase energy.<sup>40</sup> For example, Eqs. 4–7 show the combustion energies (enthalpy of combustion,  $\Delta H_c$ ), in kilojoules (kJ) per mole (mol) and kJ/g of fuel for the oxidation reactions of B, Al, and Si, respectively. The combustion enthalpy of trinitrotoluene (TNT,  $C_7H_6N_3O_6$ , Eq. 4) is also shown for comparison.<sup>52</sup>



Because of the significant gain in combustion energy (weight basis, relative to TNT) predicted by combustion calculations, B has received considerable attention as an additive to explosive and propellant mixtures.<sup>53</sup> However, practical thermodynamic and physical properties inhibit realization of this ideal.<sup>54</sup> In a

review article, Yeh and Kuo<sup>53</sup> summarized 2-stage boron-particle combustion and measured burn times. Stepwise reactions occurring in B oxidation include<sup>55</sup>



Reactions shown in Eqs. 8 and 9 are of special interest for studies of B oxidation<sup>56</sup> and the work described here because excited states of the product species are responsible for the strong visible (green) light emission, and offer the possibility of studying their emission as a function of ignition stimuli. Johns has shown<sup>29</sup> that the band structure seen in emission and fluorescence during B combustion arises from sequences of 2 electronic transitions:



A goal of this work is to map the onset of B oxidation during an explosive event.

## 4.2 Theory and Approach

---

Figure 6 shows the wavelength spectrum in emission of a burning 1:1 (by weight) mixture of a military-specification-compliant (MIL-STD-961)<sup>57</sup> B/KNO<sub>3</sub> igniter formulation. Arrows show locations of strongest observed emission bands of the BO<sub>2</sub> molecule. Off-scale features near 589 and 760 nm are emission from Na (sodium) and K (potassium) atoms, respectively. To obtain this spectrum, approximately 250 mg of the igniter formulation was placed on a resistively heated NiCr (nickel chromium) wire ribbon. When ignited, visible light emission was measured using an Ocean Optics HR2000+ spectrograph for an integration time of 100 ms after trigger. The spectrograph was externally triggered by a Si photodiode (New Focus) coupled to a Stanford Research Systems DG535 Pulse/Delay generator.

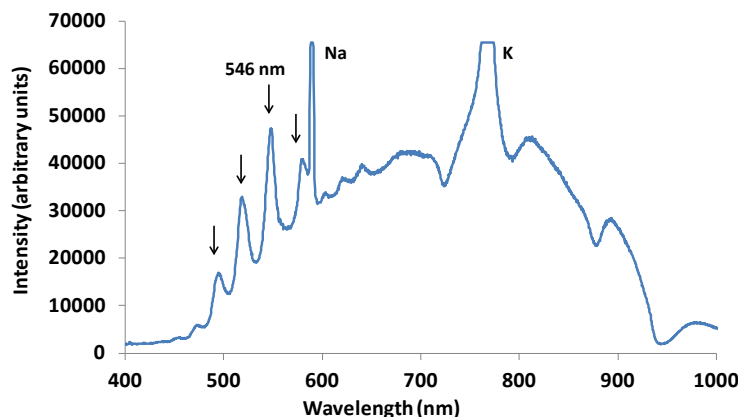


**Fig. 6** Emission from a burning 1:1 (by weight) powder mixture of a milspec B/KNO<sub>3</sub> (MIL-STD-961<sup>7</sup>) igniter formulation. Spectral lines from gaseous BO<sub>2</sub> emission (arrows) appear superimposed upon particle incandescence. Not corrected for intensity response of the spectrograph.

### 4.3 Instrumentation

The emission spectrum of burning B/KNO<sub>3</sub> shown in Fig. 6 was used as a guide to devise a scheme for imaging emission from BO<sub>2</sub> following ballistic initiation. Early-time imaging of metal oxidation products was suggested by Dreizin for AlO emission from aluminized explosives, and modified here for imaging of BO<sub>2</sub> emission (2012 December personal communication with EL Dreizin, unreferenced). Essentially, 2 light sensors (cameras), each filtered over a narrow wavelength region, observe an event over the same line of sight. The wavelength regions are selected so that one region coincides with a known emission band of the molecule of interest. The second region is selected so that it sees only particle incandescence (gray body emission).<sup>36</sup> The light signals are then ratioed to minimize the intensity from the background incandescence (subtraction gave a qualitatively similar result). For imaging BO<sub>2</sub> emission, the light sensors were 2 Phantom V7.3 monochrome cameras (Vision Research, Inc.) looking through a glass plate beam splitter (Edward Scientific) along a common line of sight. The cameras were run from the same time base (slave and master setup) using identical lenses, apertures, frame rate (typically 40 kHz), and exposure duration (typically 1 per frame rate). For measurements of BO<sub>2</sub> emission, one 50-mm-diameter filter had a bandpass (10 nm) centered at 546 nm, and the other 50-mm-diameter filter had a bandpass (10 nm) centered at 700 nm. Selection of these optical regions was based upon the spectrum shown in Fig. 6. Filters were obtained from Aurora Optical, Inc. The sensitivity of the cameras at wavelengths of 546 and 700 nm are approximately equal<sup>36</sup>; however, no correction was made to account for absolute differences in sensitivity.

#### **4.3.1 2-Camera Image Registration**

Although an effort was made to adjust the cameras to a common line of sight, it was found that a perfectly matched, hardware-based pixel-by-pixel overlap from the 2 cameras was never actually attainable. A software program was written in the computer program MATLAB to obtain a calibration image, create a transfer matrix, and then apply this matrix pixel-by-pixel to the slave-camera images. Using this software program, a fresh camera placement, and fully aligned, registered system could be achieved in approximately 10 min.

#### **4.3.2 Particle Temperature Measurements**

A 400- $\mu\text{m}$ -diameter Si-core–Si-clad optical fiber (Aurora Optics, Hanover, NH) was inserted into the top of the test chamber and the distal end coupled to an Ocean Optics HR4000 visible wavelength spectrograph. As a check, light launched into this optical fiber at the spectrograph end illuminated approximately the full volume imaged by the 2-camera rig. Therefore, any light emitted during the ballistic event within the chamber would be sampled by the spectrograph. Wavelength-resolved spectra, triggered by the gas gun firing, were recorded at 15-ms intervals during the event (timing limited by the spectrograph). To measure temperature, the Ocean Optics HR-4000 spectrograph was calibrated for intensity response using an Omega Inc. Model BB-4A calibrated blackbody. Corrected intensities reported at 850 and 990 nm were used to calculate a gray-body temperature according to the Planck function.<sup>28</sup> This wavelength region was selected because it is free from discrete spectral emission, some spectra were saturated from 650 to 800 nm, and it was decided to use a common wavelength range for all temperature calculations. A check of the temperature measurement technique using emission from an acetylene/air diffusion flame gave reasonable results (1,800 K outer soot temperature).<sup>27</sup>

#### **4.3.3 Light-Gas Gun**

The light-gas-gun facility at General Sciences Inc. (GSI, Souderton, PA) was used to investigate the impact-velocity dependence of ignition of the B/KNO<sub>3</sub>-filled polyethylene spheres. The gas gun consists of a high-pressure helium tank, a dump valve that exhausts the high-pressure gas to the gun breech, and a 25-mm-diameter, unrifled, 4.9-m-long gun barrel. The projectile, equipped with a sabot,<sup>58</sup> can achieve velocities approaching 1,200 m/s. Precise velocities are measured photonically following stripping of the sabot as the projectile exits the barrel.

KNO<sub>3</sub> powder (50- $\mu$ m particle diameter) and B powder (30- $\mu$ m particle diameter) were obtained from Fisher Scientific. The hollow 25-mm-diameter polyethylene spheres were manufactured in-house at GSI.

Following velocity measurement, the spherical projectile travels 0.5 m through free space and then enters a 50-mm-diameter, burst-disk-equipped (0.18-mm thickness, Al sheet) aperture at the near end of a 2-m<sup>3</sup> catch tank. The distal end of the cylindrical catch tank is equipped with 30-mm-thick Pyrex windows that allow visualization of the projectile impact with a steel anvil at the far interior wall of the tank. A schematic of the gas-gun catch-tank assembly is shown in Fig. 7, along with a color camera image (camera mounted to an optical port on top of the chamber) of an impact event using the B/KNO<sub>3</sub>-filled polyethylene projectile.

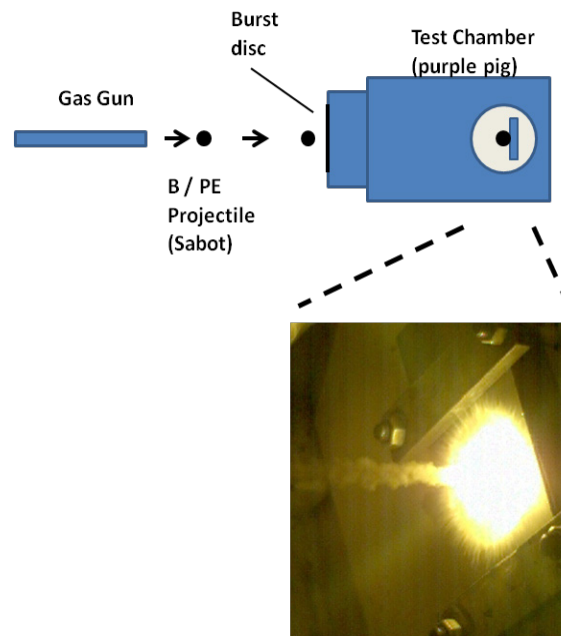


**Fig. 7** Schematic of the gas-gun catch-tank assembly. The photograph of the impact event is a single frame from a color camera mounted at the top of the catch tank assembly.

The field of view of the 2-camera rig was approximately 15 cm. The spherical polyethylene projectile weight was 1.25 g, the weight of the 1:1 by weight B/KNO<sub>3</sub> fill was 1 g ( $\pm 0.05$  g), and total projectile weight per shot was approximately 2.25 g. The 2-camera imaging rig was positioned to enable side-on imaging of the B/KNO<sub>3</sub>-filled polyethylene sphere impacting the steel anvil at the rear interior of the catch chamber. The focal plane of the 2-camera rig contained the projectile shot-axis. Figure 8 is a photograph of the catch chamber with the 2-camera rig in position at the experimental facility at GSI.

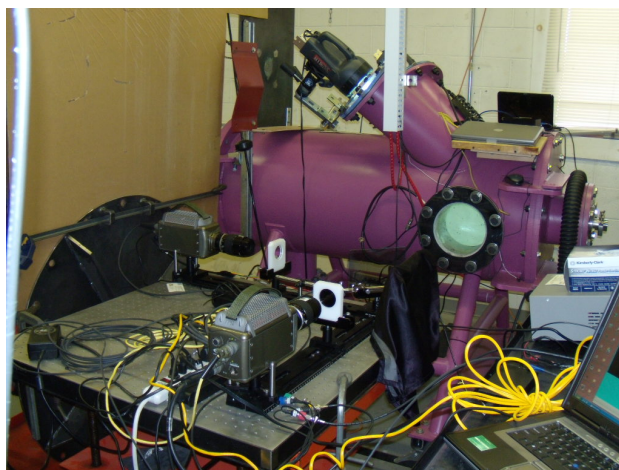


**Fig. 8** The 2-camera rig in position at the side port of the catch tank prior to a gun firing. Note the color camera at the top port of the catch tank. The gas gun is positioned to the left of the chamber out of the field of view of the photo. The white plastic fixtures in front of each camera lens contain the optical filters.

#### 4.4 Results

---

The monochrome cameras in the 2-camera rig were filtered at 546 and 700 nm (each using a 10-nm bandpass width). An examination of the emission spectrum of burning B/KNO<sub>3</sub> (Fig. 6) and comparison with measured spectral emission wavelengths for combusting B/KNO<sub>3</sub> mixtures<sup>59</sup> shows that the emission near 546 nm is a combination of incandescing hot particles and gas phase BO<sub>2</sub> emission, and the emission near 700 nm is likely due only to incandescing hot particles.

After recording a movie from each synchronized camera, and registering the images as described previously, data were prepared by doing a pixel-by-pixel ratio of intensities ( $I_{546\text{nm}}/I_{700\text{nm}}$ ) of each corresponding frame from each camera. If the ratio result was less than 1, indicating higher intensity near 700 nm, the pixel was given a red color. If the ratio result was greater than 1, indicating a higher intensity from BO<sub>2</sub> emission, the pixel was given a green color. Each frame-to-frame ratio produced a frame of a new movie (Fig. 9), consisting of green and red pixels only. The goal was to obtain a simple measure of how the impact velocity influenced the ratio of excited BO<sub>2</sub> molecules to incandescent particles.

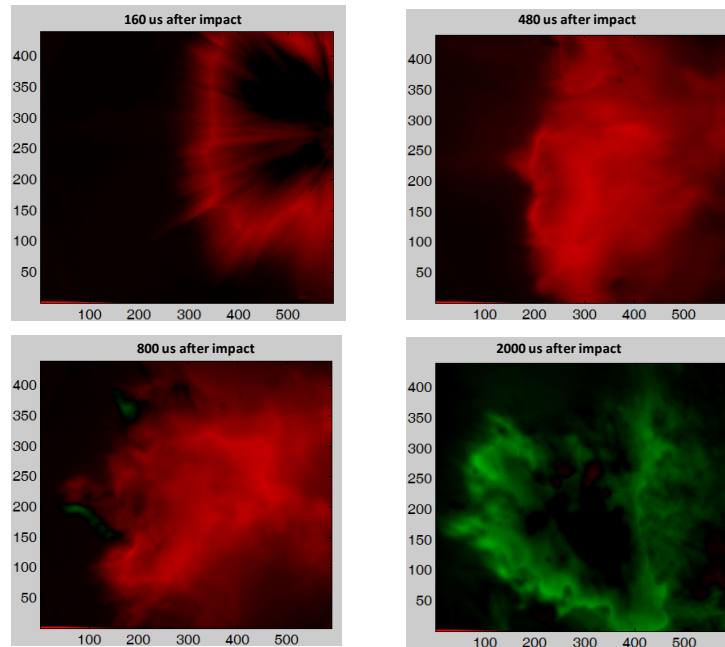


**Fig. 9** A series of processed images, time after impact, that are part of an emission movie to image B oxidation/ $\text{BO}_2$  emission. The projectile enters at the left of the figure; the anvil is at the right of the figure. Red indicates thermal emission (incandescence) near a wavelength of 700 nm has higher overall intensity; green indicates emission from incandescence plus  $\text{BO}_2$  emission near a wavelength of 546 nm has higher overall intensity. The x and y scales are pixel indices. Each pixel corresponds to approximately 100  $\mu\text{m}$  in length at the focal plane of the 2-camera rig.

To evaluate whether impact velocity has a real influence on time to appearance of  $\text{BO}_2$  emission using an arbitrary fixed ratio ( $I_{546\text{nm}}/I_{700\text{nm}} = 1$ ), it is necessary to measure the temperature of the hot particles. Figure 10 shows a plot of average particle (incandescence) temperature (850 nm, 990 nm) during time of peak  $\text{BO}_2$  emission, and time to onset of  $\text{BO}_2$  emission ( $(I_{546\text{nm}}/I_{700\text{nm}} > 1)$ ) versus impact velocity for impact experiments of B/ $\text{KNO}_3$ -containing polyethylene spheres. Shots with polyethylene spheres that did not contain the B/ $\text{KNO}_3$  mixture did not exhibit any of the discrete emission here attributed to B oxidation/ $\text{BO}_2$  emission.

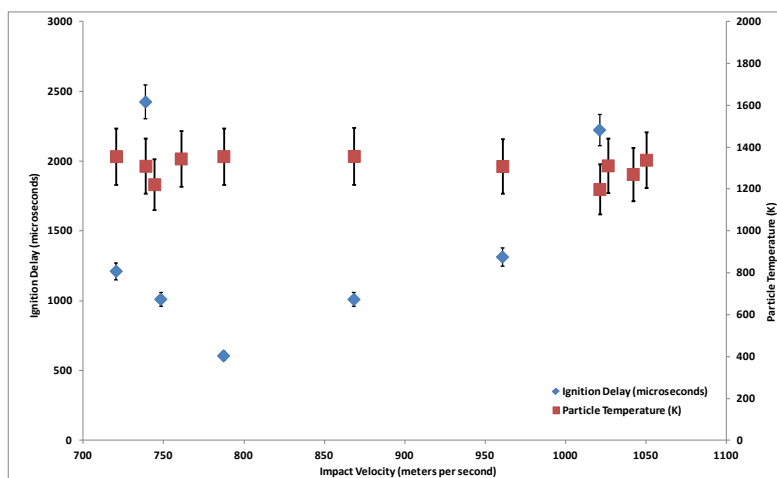


**Fig. 10** A plot of particle incandescent temperature and time to onset of gaseous  $\text{BO}_2$  emission (i.e., ignition delay) vs. impact velocity for B/ $\text{KNO}_3$ -containing polyethylene spheres

## 4.5 Discussion

Figure 10 shows that the average measured particle temperature for all experiments, during the time of most intense  $\text{BO}_2$  emission, is near 1,400 K ( $\pm 100$  K). At this temperature the intensity of  $\text{BO}_2$  gas emission/particle incandescence near 546 nm exceeds that of particulate emission intensity alone near 700 nm. In their review, Yeh and Kuo estimate the ignition of B in air to occur at approximately 1,900 K and in oxygen at approximately 1,580 K.<sup>53</sup> No data are given for ignition of B/ $\text{KNO}_3$  mixtures. The data shown in Fig. 10 indicate that onset of  $\text{BO}_2$  emission near 546 nm in the experiment described here is a direct function of particle temperature and has a more complicated dependence upon impact velocity. That is, once the powder mixture of B and  $\text{KNO}_3$  reaches approximately 1,400 K,  $\text{BO}_2$  emission becomes intense.

The data shown in Fig. 10 suggest that the imaging method described here may be of use in investigating when a metal additive participates in energy release in an energetic material formulation. The impact velocity versus onset of reaction time data shown in Fig. 10 suggest that at low velocity, there is an ignition delay during which the particle is heated to approximately 1,400 K by oxidation reactions, and the ignition delay decreases as the projectile velocity increase to 800 m/s. At higher velocities, there is an apparent rise in ignition delay with impact velocity. It is conceivable that the apparent increase in ignition delay time at impact velocities above around 850 m/s may be caused by the hottest particles leaving the camera field of view as these particles are expected to have high velocities relative to particles produced at lower impact velocities. This suggests a sweet spot, or an optimum impact velocity for minimizing time to onset of B oxidation with these experimental parameters for the field of view achieved with the 2-camera rig.



Additionally, although it is implied that the onset of green pixels in the individual images indicates ignition delay times, the onset of green pixels actually means that the intensity of emission at 546 nm, at this time after impact, exceeds that of incandescent emission at 700 nm. For the data shown in Fig. 10, the projectile velocity at impact is believed to have an error approaching 10%, the uncertainty in time to BO<sub>2</sub> emission is believed to be approximately 100  $\mu$ s, and the error in calculated temperature is believed to be approximately 100 K, based upon calibration measurements using emission from an acetylene/air flame.

## **5. Blast Energy on Target**

---

### **5.1 Introduction**

---

High-speed wavelength-filtered imaging, in combination with pulsed laser illumination, has been used previously<sup>45</sup> to image shock waves near the expanding detonation products. Recently, a new effort was initiated to measure blast energy on target. This program measures incoming and reflected blast waves, determines the energy in each, and from the difference determines blast energy imparted to a target. To accomplish this, an enhancement in fidelity of blast wave imaging was needed.

### **5.2 Instrumentation**

---

Figure 11 shows a schematic of a low-parallax high-brightness imaging rig (LP-HBI) developed for this effort, which is used to image incoming and reflected shock waves. A method to measure the blast energy deposited on the target is to calculate the initial energy per gram of shocked air in the incident shock wave and the energy per gram in the reflected shock wave immediately before and after the encounter with the visor. These energies are calculated using only the peak pressure of the respective waves. The difference is assumed to be the energy absorbed by the target at the peak incident pressure and is expressed as a percentage of the peak incident energy per gram. This percentage is assumed to apply to the total impulse of the incident wave.



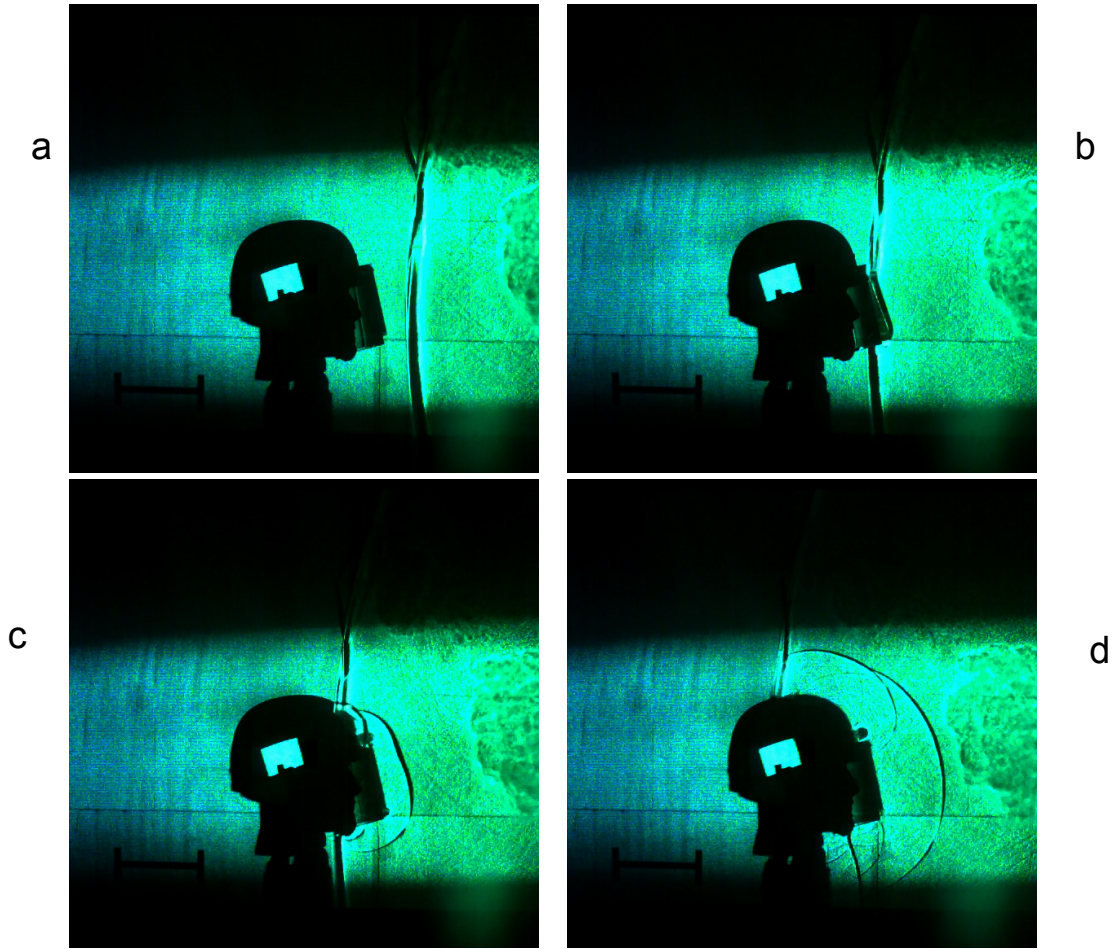


**Fig. 12** A shock wave being reflected by a mannequin. Peak pressure at the visor was approximately 69.5 psi. Charge was 660-g pentolite, 2 m from center of face shield.

## 5.4 Results

To calculate the energy imparted to the target, the required inputs<sup>52</sup> are as follows:

- Measured incident ( $U_1$ ) and reflected ( $U_2$ ) shock velocities
- Hugoniot for air

The incident and reflected shock velocities were calculated from sequential Photron SA-5 images (Fig. 12 and Table 1). Time of images in Fig. 12 is  $a < b < c < d$ . The air Hugoniot<sup>61</sup> can be expressed as a relation between the shock ( $U_1$ ) and particle ( $u_1$ ) velocities in meters per second for air at a density ( $\rho_0$ ) of  $1.29 \text{ kg/m}^3$  or specific volume,  $V_0$ , of  $0.775 \text{ m}^3/\text{kg}$ .

$$U_1 = 0.2425 + 1.1231u_1 \quad (12)$$

The incident shock overpressure may be given by<sup>52</sup>

$$P_1 - P_0 = \rho_0 U_1 u_1 = (1.29 \text{ kg/m}^3)(705.2 \text{ m/s})(411.9 \text{ m/s}) = 374708.7 \text{ Pa} . \quad (13)$$

Units of pressure are Pascals (Pa),  $P_0=101,325 \text{ Pa}$  and  $P_1$  = absolute shock pressure. Using these relationships, the incident peak pressure on the visor in Figure 12b is approximately 476,033.7 Pa, or 68.6 psi.

The initial specific volume,  $V_0= 1/(0.00129 \text{ kg/m}^3) = 0.775 \text{ m}^3/\text{kg}$ . The shocked specific volume,  $V_1$ , may be given by<sup>62</sup>

$$V_1 = 0.775(U_1 - u_1)/U_1 = 0.322 \text{ m}^3/\text{kg} . \quad (14)$$

From Cooper,<sup>52</sup> the energy equation for a shock moving into unshocked air is

$$E_2 = 1/2(P_1 + P_0)(V_0 - V_1) + 1/2(u_1)^2 . \quad (15)$$

For the incident shock shown in Fig. 12b, this yields a specific volume shock energy of 215.6 kilojoules per kilogram (kJ/kg). A summary of physical parameters of the shock prior to the visor is shown in Table 1.

**Table 1 Physical parameters of the shock prior to visor**

$U_1$ (m/s)	$u_1$ (m/s)	$V_0$ (m <sup>3</sup> /kg)	$V_1$ (m <sup>3</sup> /kg)	$P_0$ (Pa)	$P_1$ (Pa)	$E_1$ (kJ/kg)
705.2	411.9	0.775	0.322	101,325	476,033.7	215.6

After encountering the visor, the portion of the incident shock that is reflected will travel back through preshocked air. Relative to ambient conditions, this air has a higher density and a particle velocity,  $u_1$ , caused by the incident shock. The particle velocity in the preshocked air ( $u_1$ ) is added to the observed reflected shock velocity ( $U_r$ ) to get the true propagation velocity of the reflected wave at the moment of reflection into the shocked air,  $U_2$ .

$$U_r + u_1 = U_2 = 366.7 \text{ m/s} + 411.9 \text{ m/s} = 778.6 \text{ m/s} . \quad (16)$$

From the full image sequence of the experiments, it was ascertained that there was no perceptible motion of the visor after impact, indicating that the particle velocity of the air was essentially zero behind the reflected shock. The change in particle velocity,  $du_1$ , is then equal to  $u_1$ .

The reflected shock travelled into air with a specific volume imparted by the incident shock. The specific volume of air behind the incident shock,  $V_2$ , is given by

$$V_2 = (V_1)(U_r/U_2) = (0.322 \text{ m}^3/\text{kg})(366.7 \text{ m/s} / 778.6 \text{ m/s}) = 0.152 \text{ m}^3/\text{kg}. \quad (17)$$

The reflected shock overpressure is then calculated as in Eq. 13.

$$\begin{aligned} P_2 - P_1 &= \rho_1 U_2 u_1 = (1/V_1)(U_2)(du_1) = (3.11 \text{ kg/m}^3)(778.6 \text{ m/s})(411.9 \text{ m/s}) \\ &= 997,393.6 \text{ Pa} . \end{aligned} \quad (18)$$

The reflected energy per gram,  $E_2$ , is equal to the change in internal energy per gram plus kinetic energy per gram.

$$E_2 = 1/2(P_2 + P_1)(V_1 - V_2)(10^6) + 1/2(u_1(10^5))^2 \text{ (kJ/kg)}. \quad (19)$$

$$E_2 = 1/2(1949461 \text{ Pa})(0.17 \text{ m}^3/\text{kg}) = 165.7 \text{ kJ/kg}. \quad (20)$$

A summary of physical parameters of the shock after reflection by the visor is shown in Table 2. This analysis, although preliminary, indicates that for the target assembly shown in Fig. 12 (mannequin plus visor), the reflected shock contained 77% of the energy of the incident shock. Therefore, the target assembly experienced approximately 23% of the initial shock energy. Figure 13 shows a plot of incoming versus reflected shock velocity for the shock/mannequin interaction shown in Fig. 12.

**Table 2 Physical parameters of the shock after reflection by visor**

$U_r$ (m/s)	$du$ (m/s)	$u_1$ (m/s)	$u_2$ (m/s)	$V_1$ (m <sup>3</sup> /kg)	$V_2$ (m <sup>3</sup> /kg)	$P_1$ (Pa)	$P_2$ (Pa)	$E_2$ (kJ/g)
366.7	411.9	411.9	0	0.322	0.152	476,033.7	1473,427.3	165.7

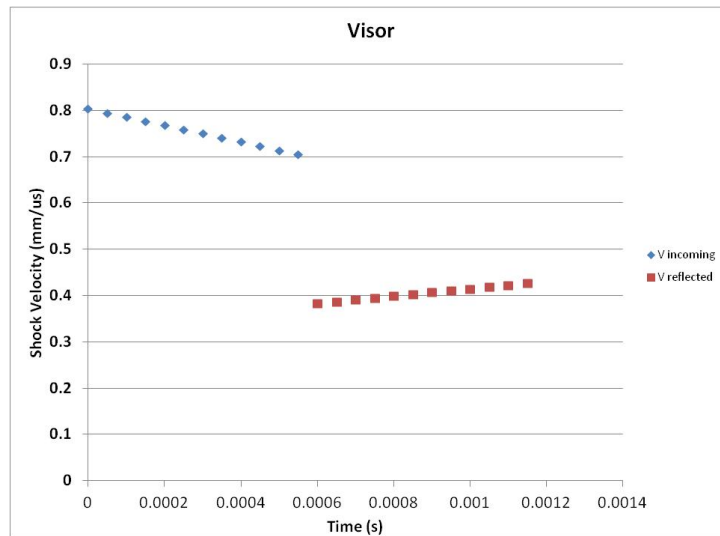


**Fig. 13 Incoming vs. reflected shock velocity for Fig. 8.**

## 6. Summary and Conclusions

The work described here indicates that high-speed high-fidelity imaging incorporating optical filtering and signal processing techniques can make a significant contribution to analysis of the behavior of high explosives. The data generated using these techniques have applicability to explosives and munitions formulation and design and to improving soldier protection. The ability to simultaneously create temperature, peak pressure, and chemical species maps of explosions offers experimental measurements that rival or exceed fidelity achievable through simulation and, therefore, represents an important development in model validation. Additionally, generating a full data set in standoff mode for a single shot improves cost-effectiveness of funding dollars earmarked for experimentation.

The fidelity and dimensionality achieved using these new methods should prove useful in determining performance of new disruptive energetics and insensitive munitions and in determining the real utility of fuel additives to explosives. This work demonstrates a standoff tool to characterize explosive performance that rivals present modelling capabilities, and should provide validation data for physical chemical explosives models that incorporate finite rate chemical kinetics.

## 7. References

---

1. Michalski L, Eckersdorf K, Kucharski J, McGhee J. Temperature measurement. 2nd ed. West Sussex (England): John Wiley & Sons Ltd; 2001.
2. Waidner CW, Burgess G K. Optical pyrometry. In: Scientific papers of the bureau of standards, no. 11. Washington (DC): Government Printing Office; 1905.
3. Motzfeldt K. High temperature experiments in chemistry and materials science. Chichester (UK): John Wiley and Sons Ltd; 2013.
4. Kostkowski HJ, Lee RD. Theory and methods of optical pyrometry. Natl Bur Stand Monogr 41. Washington (DC): National Bureau of Standards; 1962 Mar 1; p. 361–390.
5. Balaji C. Essentials of radiation heat transfer. West Sussex (England): John Wiley & Sons Ltd; 2014.
6. Ogura T, Okada K, Abe T, Wakabayashi K, Ishikawa K, Kuroda E, Matsumura T, Nakayama Y, Yoshida M. Pyrometry study on fireballs generated upon the explosion of TNT. In: Energetic materials: reactions of propellants, explosives and pyrotechnics. Proceedings of the 34th International Annual Conference of ICT; 2003 June 24–27; Karlsruhe, Germany. Karlsruhe (Germany): Fraunhofer-Institut für Chemische Technologie; 2003. p. 18/1.
7. Goroshin S, Frost DL, Levine J, Yoshinaka A, Zhang F. Optical pyrometry of fireballs of metalized explosives. Propellants, Explosives, Pyrotechnics. 2006;31(3):169–181.
8. Capitelli M, Colonna G, D’Ammando G, Gaudioso R, and Pietanza LD. Physical processes in optical emission spectroscopy. In: Musazzi S, Perini U, editors. Laser induced breakdown spectroscopy: theory and applications. Heidelberg (Germany): Springer; 2014.
9. McNesby KL, Fifer RA. Rotational temperature estimation of CO at high temperatures by graphical methods using FT-IR spectroscopy. Applied Spectroscopy. 1997;45:61–67.
10. Bédard B, Giovannini A, Pauzin S. Thin filament infrared pyrometry: instantaneous temperature profile measurements in a weakly turbulent hydrocarbon premixed flame. Exp Fluids. 1994;17:397–404.

11. Fu T, Cheng X, Yang Z. Theoretical evaluation of measurement uncertainties of two-color pyrometry applied to optical diagnostics. *Applied Optics*. 2008;47(32):6112–6123.
12. Hampson GJ, Reitz RD. Two-colour imaging of incylinder soot concentration and temperature in a heavy-duty DI diesel engine with comparison to multidimensional modeling for single and split injections. Warrendale (PA): Society of Automotive Engineers; 1998. SAE Tech. Paper 980524.
13. Cignoli F, De Iuliis S, Manta V, Zizak G. Two-dimensional two-wavelength emission technique for soot diagnostics. *Appl Opt*. 2001;40:5370–5378.
14. Connelly BC, Kaiser SA, Smooke MD, Long MB. Two-dimensional soot pyrometry with a color digital camera. In: *Proceedings of the Fourth Joint Meeting of the US Sections of the Combustion Institute*; March 2005; Philadelphia, PA. Pittsburgh (PA): Combustion Institute; 2005.
15. Kuhn PB, Blair BM, Connolly C, Smooke MD, Long MB. Soot and thin-filament pyrometry using a color digital camera. *Proceedings of the Combustion Institute*. 2011;33(1):743–750.
16. Densmore JM, Homan BE, Biss MM, McNesby, KL, High-speed two-camera imaging pyrometer for mapping fireball temperatures. *Appl Opt*. 2011;50(33):6267-6271.
17. Densmore JM, Biss MM, McNesby, KL, Homan BE. High speed digital color imaging pyrometry. *Appl Opt*. 2011;50(17):2659–2665.
18. Alberty RA, Daniels F. *Physical chemistry*. 5th ed. New York (NY): John Wiley and Sons; 1979.
19. Densmore JM, Biss MM, Homan BE, McNesby KL. Thermal imaging of nickel-aluminum and aluminum-polytetrafluoroethylene impact initiated combustion. *Journal of Applied Physics*. 2012;112(8):084911–084911-5.
20. McNesby K, Homan B, Piehler T, Lottero R. Spectroscopic measurements of fireballs produced by enhanced blast explosives. Aberdeen Proving Ground (MD): Army Research Laboratory (US); 2004. Report No. ARL-TR-3318.
21. McNesby KL, Homan BE, Ritter JJ, Quine Z, Ehlers RZ, McAndrew BA. Afterburn ignition delay and shock augmentation in fuel rich solid explosives. *Propellants, Explosives, Pyrotechnics*. 2010;35(1):57–65.
22. Wien W. On the division of energy in the emission-spectrum of a black body. *Philosophical Magazine*. 1897;5:43(262):214–220.



23. Densmore JM, Biss MM, Homan BE, McNesby KL. Evaluation of reactive-material-surrounds explosive charges. Aberdeen Proving Ground (MD): Army Research Laboratory (US); 2011 July. Report No. ARL-TR-5603.
24. Kuhl AL, Forbes JJ, Chandler AK, Oppenheim R, Spektor Ferguson RE. Confined combustion of TNT explosion products in air. In: Proceedings of the 8th International Colloquium on Dust Explosions, 1998 Sep 21–25, Schaumburg, IL.
25. McNesby KL, Miziolek AW, Nguyen T, Delucia FC, Skaggs RR, Litzinger TA. Experimental and computational studies of oxidizer and fuel side addition of ethanol to opposed flow air/ethylene flames. *Combustion and Flame*. 2005;142:413–427.
26. McNesby KL, Biss MM, Benjamin RA, Thompson RA. Chemical imaging of explosions – mapping  $\text{BO}_2$  light emission. *Propellants, Explosives, Pyrotechnics*. 2015;40(4):539–543.
27. Sivathanu YR, Faeth GM. Temperature/soot volume fraction correlations in the fuel-rich region of buoyant turbulent diffusion flames. *Combustion and Flame*. 1990;81:150–165.
28. Herzberg G. Molecular spectra and molecular structure II. Infrared and Raman spectra of polyatomic molecules. New York (NY): D Van Nostrand Company, Inc; 1950.
29. Johns JWC. The absorption spectrum of  $\text{BO}_2$ . *Canadian Journal of Physics*. 1961;39:1738–1768.
30. Volan A, Alati L. A new optical pressure measurement system. Proceedings of the 14th International Congress Instrumentation in Aerospace Simulation Facilities (ICIASF); 1991 Oct 27–31, Rockville, MD. New York (NY): Institute of Electrical and Electronics Engineers; 1991. p 10–16.
31. Barnett JD, Block S, Piermarini GJ. An optical fluorescence system for quantitative pressure measurement in the diamond-anvil cell. *Rev Sci Instrum*. 1973;44(1):1–9.
32. Wagner C, Frankenberger J, Deimel PP. Optical pressure sensor based on a Mach-Zehnder interferometer integrated with a lateral a-Si:H p-i-n photodiode. *IEEE Photonics Technology Letters*. Oct 1993;5(10):1257–1259.
33. Glenn WH, Tomlinson RG, inventors; United Technologies Corporation, assignee. Optical pressure sensor. United States Patent US 4,368,645 A. 1983 Jan 18.

34. Hocker GB. Fiber-optic sensing of pressure and temperature. *Applied Optics*. 1979;18(9):1445–1448.
35. Philippe LC, Hanson RK. Laser diode wavelength-modulation spectroscopy for simultaneous measurement of temperature, pressure, and velocity in shock-heated oxygen flows. *Applied Optics*. 1993;32(30):6090–6103.
36. Settles GS. Schlieren and shadowgraph techniques – visualizing phenomena in transparent media. Berlin (Germany): Springer; 2001.
37. Mach E, Salcher P. Photographische fixierung der durch projectile in der luft eingeleiteten vorgange. *Sitzungsb Akad Wiss Wien*. 1887;95:764–780.
38. Cranz C, Schardin H. Kinematographie auf ruhendem film und mit extreme hoher bildfrequenz. *Zeitschrift fur Physic*. 1929;56:147–183.
39. Merzkirch, W. Flow visualization. 2nd ed. New York (NY): Academic Press; 1987.
40. Eyles ED. High-speed photography and its applications to industrial problems. *J Sci Instruments*. 1941;18:175–184.
41. Kinney GF, Graham KJ. Explosive shocks in air. 2nd ed. Berlin (Germany): Springer-Verlag; 1985.
42. Biss M, McNesby K. Optically measured explosive impulse. *Experiments in Fluids*. 2014;55:1749.
43. Watts DB, Van Tassel MT. Remote blast pressure sensor. Eglin Air Force Base (FL): Air Force Armament Laboratory (US); 1988 Aug. Report No.: A7ATL-88-55.
44. Dosser LR, Reed JW, Stark MA. High-speed photography of energetic materials and components with a copper vapor laser. *MRS Proceedings*, Vol. 117, 1988. p. 239. doi:10.1557/PROC-117-239.
45. Frost DL, Goroshin S, Levin J, Ripley R, Zhang F. Critical conditions for ignition of metal particles in a condensed explosive. *Proceedings of 12th International Detonation Symposium*; 2002 August 11–16; San Diego, CA. Arlington (VA): Office of Naval Research. Report No.: ONR 333-05-2. p. 693–701.
46. McNesby KL, Homan BE, Lottero RE. High brightness imaging for real time measurement of shock, particle, and combustion fronts produced by enhanced blast explosives. Aberdeen Proving Ground (MD): Army Research Laboratory (US); 2005 Jan. Report No.: ARL-TR-3411.

47. Walter PL. Introduction to air blast measurements PCB Tech note TN-12. Depew (NY): PCB Peizotronics. [accessed 2015 July 2].  
[http://www.pcb.com/techsupport/docs/prs/TN-12-0904\\_Air\\_Blast\\_Part\\_1.pdf](http://www.pcb.com/techsupport/docs/prs/TN-12-0904_Air_Blast_Part_1.pdf).
48. Watts DB, Van Tassel MT. Transducer development for explosive measurements. Eglin Air Force Base (FL): Air Force Armament Laboratory (US); 1989. Report No.: AFATL-TP-89-12.
49. Nelson BN, Gallagher MD. Ultrahigh frequency pressure sensors. Newton (MA): Geocenters, Inc; 1988 Oct. Report No.: AFATL-TR-88-49.
50. McNesby KL, Biss MM, Benjamin RA, Thompson RA. Optical measurement of peak air shock pressures following explosions. *Propellants, Explosives, Pyrotechnics*. 2013;35:1–6.
51. Hyde D. User's guide for microcomputer programs: CONWEP and FUNPRO—applications of TM 5-855-1. Vicksburg (MS): Army Engineer Waterways Experimental Station (US); 1988.
52. Cooper PW. Explosives engineering. New York (NY): Wiley-VCH, Inc; 1996.
53. Yeh CL, Kuo KK. Ignition and combustion of boron particles. *Prog Energy Combust Sci*. 1996;22:511–541.
54. Miller WJ. Boron combustion product chemistry. Princeton (NJ): AeroChem Research Laboratories; 1976 Oct. Report No.: TP-349.
55. Brown RC, Kolb CE, Cho SY, Yetter RA, Dryer FL, Rabitz H. Kinetic model for hydrocarbon-assisted particulate boron combustion. *Int Journal of Chem Kinet*. 1994;26(3):319–332.
56. Dreizin EL, Keil DG, Felder W, Vicenzi EP. Phase changes in boron ignition and combustion. *Combustion and Flame*. 1999;119:272–290.
57. MIL-STD-961E. Department of defense standard practice: defense and program-unique specifications format and content. Fort Belvoir (VA): Defense Standardization Program Office; 2003 Aug 1.
58. Burns BP, Burton L, Drysdale WH. Methodologies for forecasting sabot mass for advanced gun and projectile systems. Aberdeen Proving Ground (MD): Army Ballistic Research Laboratory (US); 1992. Report No.: BRL-TR-3387.
59. Snowden BS Jr. The emission spectrum of the  $\text{BO}_2$  molecule. Thesis 64-4757 [PhD physical chemistry thesis]. [University Microfilms, Inc., Ann Arbor, (MI)]: Vanderbilt University; 1963.

60. Kohler J, Meyer R. Explosives. 4th ed. New York (NY): VCH Publishers; 1993.
61. Zukas JA, Walters WP, editors. Explosive effects and applications. New York (NY): Springer; 1997. Chapter 3.
62. Mader CL. Numerical modeling of explosives and propellants. 3rd ed. Boca Raton (FL): CRC Press; 2008.

1 DEFENSE TECHNICAL  
(PDF) INFORMATION CTR  
DTIC OCA

2 DIRECTOR  
(PDF) US ARMY RESEARCH LAB  
RDRL CIO LL  
IMAL HRA MAIL & RECORDS MGMT

1 GOVT PRINTG OFC  
(PDF) A MALHOTRA

1 DIR USAR  
(PDF) RDRL WML C  
K MCNESBY

INTENTIONALLY LEFT BLANK.